frontiers in Astronomy and Space Sciences

ORIGINAL RESEARCH
published: 09 June 2021
doi: 10.3389/fspas.2021.660992

Characterizing Spectral Channels of Visible Emission Line Coronagraph of Aditya-L1

Ritesh Patel[1,2]*, *A. Megha*[1], *Arpit Kumar Shrivastav*[1,2,3], *Vaibhav Pant*[2]*, *M. Vishnu*[1], *K. Sankarasubramanian*[1,4,5] *and Dipankar Banerjee*[1,2,4]

[1]*Indian Institute of Astrophysics, Bangalore, India,* [2]*Aryabhatta Research Institute of Observational Sciences, Nainital, India,* [3]*Department of Physics, Indian Institute of Science, Bangalore, India,* [4]*Center of Excellence in Space Science, IISER Kolkata, Kolkata, India,* [5]*UR Rao Satellite Centre, Bangalore, India*

Aditya-L1 is India's first solar mission with the Visible Emission Line Coronagraph (VELC), which consists of three spectral channels taking high-resolution spectroscopic observations of the inner corona up to 1.5 $R_\odot$ at 5,303, 7,892, and 10,747 Å. In this work, we present a strategy for the slit width optimization of the VELC using synthetic line profiles by taking into account the instrument characteristics and coronal conditions for log(T) varying from 6 to 6.5. The synthetic profiles are convolved with simulated instrumental scattered light and noise to estimate the signal-to-noise ratio (SNR), which will be crucial to designing the future observation plans. We find that the optimum slit width for VELC turns out to be 50 µm, providing sufficient SNR for observations in different solar conditions. We also analyzed the effect of plasma temperature on the SNR at different heights in the VELC field of view for the optimized slit width. We also studied the expected effect of the presence of a CME on the spectral channel observations. This analysis will help to plan the scientific observations of VELC in different solar conditions.

Keywords: Corona, coronagraph, spectroscopy, emission lines, instrumentation

OPEN ACCESS

Edited by:
Edward M. B. Thiemann, University of Colorado Boulder, United States

Reviewed by:
Su-Chan Bong, Korea Astronomy and Space Science Institute, South Korea
Joan Burkepile, National Center for Atmospheric Research (UCAR), United States

***Correspondence:**
Ritesh Patel
ritesh.patel@iiap.res.in
Vaibhav Pant
vaibhav.pant@aries.res.in

Specialty section:
This article was submitted to Stellar and Solar Physics, a section of the journal Frontiers in Astronomy and Space Sciences

Received: *30 January 2021*
Accepted: *12 May 2021*
Published: *09 June 2021*

Citation:
Patel R, Megha A, Shrivastav AK, Pant V, Vishnu M, Sankarasubramanian K and Banerjee D (2021) Characterizing Spectral Channels of Visible Emission Line Coronagraph of Aditya-L1. Front. Astron. Space Sci. 8:660992. doi: 10.3389/fspas.2021.660992

1 INTRODUCTION

The observations of the inner corona (up to 3 $R_\odot$) in white-light and emission lines have been made during total solar eclipses over the years, yielding a detailed description of the corona (Baumbach, 1937; van de Hulst, 1950; Habbal et al., 2007, 2010; Habbal et al., 2014; Boe et al., 2018). During total solar eclipses, spectroscopic investigations using the emission lines detected the presence of oscillations and fast magnetohydrodynamic (MHD) waves in the solar atmosphere (Singh et al., 1997; Pasachoff et al., 2002; Sakurai et al., 2002; Singh et al., 2011; Samanta et al., 2016). As eclipses last for a couple of minutes, regular observations of the inner corona will help improve our understanding of the solar atmosphere. It may also shed light on the development of small- and large-scale transients that lead to severe space weather. The availability of observations in emission lines such as Hα 6563 Å, Fe IX 4359 Å, Fe X 6374 Å, Fe XI 7892 Å, Fe XIII 10747 Å, Fe XIV 5303 Å, and Ni XV 6702 Å can provide useful thermodynamic diagnostics of the different processes occurring in the solar corona (Habbal et al., 2011). It should be noted that current ground- and space-based instruments lack coronal observations in the majority of these wavelengths. The Coronal Multi-channel Polarimeter (CoMP) instrument (Tomczyk et al., 2008) in the Mauna Loa Solar Observatory (MLSO) provided regular spectropolarimetric observations of the inner corona up to

1.5 $R_\odot$ at 10,747 and 10,798 Å until 2018. The detection of Alfvénic waves in the solar corona using the CoMP data provided support for wave-based models for coronal heating (Tomczyk et al., 2007; Morton et al., 2015; Morton et al., 2016; Morton et al., 2019). The observations made using this instrument also provided the first global magnetic map of the solar corona (Yang et al., 2020). Another ground-based instrument, the Norikura coronagraph, located at Norikura, Japan, provided spectroscopic observations of the off-limb corona in emission lines corresponding to Fe X, Fe XI, Fe XIII, and Fe XIV. The emission line–intensity ratios give an estimate of the temperature, while the line width could be used to calculate the thermal and nonthermal structure of the emitting plasma. Such high-resolution spectroscopic observations from Norikura and CoMP revealed the thermal and nonthermal variations in coronal structures and velocities, complex variations in line–intensity ratios inferring the distribution of multi-thermal plasma, and turbulence in these structures (Singh et al., 2003; Singh et al., 2004; Singh et al., 2006a; Singh et al., 2006b; McIntosh and De Pontieu, 2012; Prasad et al., 2013; Morton et al., 2016; Fan et al., 2018; Pant et al., 2019; Tiwari et al., 2019).

The variations in the temperature and nonthermal velocity in coronal structures may give an insight into the processes involved in heating the corona and the acceleration of the solar wind. Therefore, continuous spectroscopic monitoring of the solar corona in such emission lines is required. Among the existing space-based spectrograph instruments, the EUV Imaging Spectrometer (EIS) on Hinode observes the solar corona and the upper transition region in the wavelength range of 170–210 Å and 250–290 Å (Culhane et al., 2007). Another spacecraft, the Interface Region Imaging Spectrograph (IRIS), takes simultaneous imaging and spectroscopic observations of the photosphere, chromosphere, transition region, and corona in three passbands of 1,332–1,358 Å, 1,389–1,407 Å, and 2,783–2,834 Å (De Pontieu et al., 2014). The Spectral Imaging of the Coronal Environment (SPICE) instrument (SPICE Consortium et al., 2020) onboard the recently launched Solar Orbiter is an imaging spectrometer capable of observing the corona in extreme ultraviolet (EUV) passbands of 70.4–79.0 nm and 97.3–104.9 nm. It should be noted that EIS, IRIS, and SPICE perform the observations confined to a small field of view (FOV).

The Visible Emission Line Coronagraph (VELC) onboard Aditya-L1 (Seetha and Megala, 2017) will take simultaneous imaging and spectroscopic observations of the inner solar corona in three visible and one infrared (IR) passband from 1.05 to 1.5 $R_\odot$ (Singh et al., 2013; Banerjee et al., 2017; Raghavendra Prasad et al., 2017). VELC is equipped with a multi-slit spectrograph to study the solar corona with high spatial and temporal resolutions in the three emission lines centered at 5,303 Å (Fe XIV), 7,892 Å (Fe XI), and 10,747 Å (Fe XIII), mostly used during the eclipse observations. The continuous observations provided by VELC will be helpful in attaining its scientific objectives, including the diagnostics of the coronal plasma for temperature and velocity, thereby understanding the process of coronal heating and the acceleration of the solar wind. Moreover, the spectropolarimeteric capability of VELC using the 10,747 Å emission line will be helpful in directly estimating the magnetic fields of the solar corona. Therefore, it is necessary to understand the performance of the instrument beforehand to plan the observations after launch.

In this article, we present the characterization of the VELC spectral channels using synthetic spectra generated using CHIANTI 8.0 for different coronal conditions, taking the instrument parameters into account. In **Section 2**, we present the process involved in synthesizing the spectra and converting it to simulated observations. We present a detailed analysis and the results including the optimization of the slit width of VELC, followed by the instrument performance for different conditions, in **Section 3**. **Section 4** summarizes the analysis, followed by a discussion.

2 SYNTHESIZING SPECTRA

As discussed before, VELC will take spectroscopic observations of the inner corona at three emission wavelengths centered at 5,303, 7,892, and 10,747 Å. We used the CHIANTI 8.0 atomic database (Dere et al., 1997; Del Zanna et al., 2015) to generate emission spectra for these three ionization states of iron. It should be noted that the mechanism responsible for the emission corona is atomic transitions, unlike the scattering of photospheric light in the case of the K and F corona. Also, it has been found that the F corona dominates beyond 2.5–3 $R_\odot$ (Morgan and Habbal, 2007), which is beyond the VELC field of view (FOV) of the spectroscopic channels. The emission lines under consideration are about 100 times brighter than the background K continuum (Stix, 2002). We have included the continuum while preparing the synthetic spectra with CHIANTI. The contribution of the instrument to the full width half maximum (FWHM) of the spectra is calculated using the following relation:

$$\mathrm{FWHM}_{\mathrm{instr}} = \sqrt{\left(\frac{\mathrm{dispersion}}{\mathrm{pixel\ scale}} \times \mathrm{slit\ scale}\right)^2 + (\mathrm{dispersion})^2}, \quad (1)$$

where "dispersion" corresponds to 28.4, 31, and 227.3 mÅ/pixel for the three channels, respectively (Singh et al., 2019). A pixel size of 6.5 μm for the visible spectral channels and 25 μm for the IR channel result in pixel scales of 1.25 arcsec pixel^{-1} and 4.8 arcsec pixel^{-1}, respectively. It should be realized from the optical layout of VELC (Figure 1 in Kumar et al., 2018) that the set of four slits in the slit plane placed in the optical path is incident on the spectrograph. We vary the slit width as 20, 40, and 60 μm and investigate their effects on the instrument output (see **Section 3**). The density and emission measures for the different scenarios are supplied as inputs to CHIANTI. The synthetic spectra are computed using IDL procedures of CHIANTI, *ch_synthetic.pro* and *make_chianti_spec.pro*. The instrumental FWHM calculated using **Eq. 1** is provided as an input to *make_chianti_spec.pro* for the instrument-induced FWHM to the synthetic line. The peak of

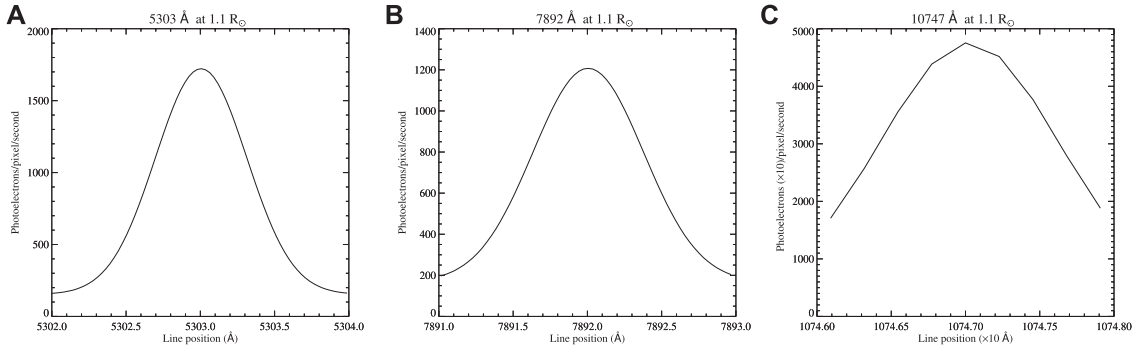

FIGURE 1 | Synthetic spectra for VELC at 1.1 $R_\odot$ for **(A)** 5,303 Å, **(B)** 7,892 Å, and **(C)** 10,747 Å for 50 μm slit width at their respective line formation temperatures. Photons due to instrument scattering are added to the spectra.

the intensity obtained, which has the physical unit of photons cm^{-2} sr^{-1} s^{-1} $Å^{-1}$, is then converted to equivalent photoelectrons incident on each pixel per second using the following relation:

$$\text{ph\_elecs}_{\text{peak}} = (\text{peak intensity}) \times \text{area} \times (\text{solid angle}) \times \text{dispersion} \times \text{efficiency ph.electrons/pixel/s}, \quad (2)$$

where the area of the VELC primary is obtained by taking the diameter of the primary mirror as 195 mm (Kumar et al., 2018). The solid angle subtended is calculated using the slit scale and pixel scale along the horizontal and vertical dimensions, respectively. The efficiency of the spectral channels in the visible and IR wavelengths is taken to be ~5 and ~4%, respectively (Singh et al., 2019).

The instrument contribution to the scattered intensity and noise arising due to the detector is also included in the simulated spectra. Scatter studies for the continuum channel of VELC (observing at 5,000 Å with the 10 Å passband) were carried out using Advanced System Analysis Program (ASAP) by Venkata et al. (2017). As VELC has narrowband filters for the three channels, we scaled these scattered intensity values, taking into account the passband of individual channels. The scatter of the continuum was scaled to the spectral channels using the following equation:

$$\text{scatter}_{\text{spec}} = \frac{\text{dispersion}}{10} \times \frac{\text{slit scale} \times (\text{pixel scale})_{\text{spectral}}}{(\text{pixel scale})^2_{\text{continuum}}} \times (\text{Scatter}_{\text{continuum}})\ \text{ph.electrons}\Big/\text{pixel/s}, \quad (3)$$

which gives the number of scattered photoelectrons in the spectral channel generated in a pixel every second. The pixel scale for the continuum channel is 2.5 arcsec $pixel^{-1}$. The constant factor in **Eq. 3** is obtained using the procedure for conversion followed by Patel et al. (2018). The scatter is assumed to be circularly symmetric and is added to the synthetic spectra obtained using CHIANTI in **Eq. 2**. This could be considered as the worst case scenario as scatter is inversely related to the square of the incident wavelength. The final spectra obtained are then used for further analysis.

3 ANALYSIS AND RESULTS

The synthetic spectra for each channel are added with the dark noise associated with individual detectors. For the visible spectral channels using the CMOS detector, the dark noise (D) is up to 15 electrons, whereas in the high-gain mode of the IR CCD, it is 42 electrons, with a readout noise (R) of 2 and 80 electrons, respectively (Singh et al., 2019, VELC team). The photon noise (p) is calculated as the square root of the total photoelectrons generated, including the coronal signal photons obtained in the spectra and the scattered photons. The resulting signal-to-noise ratio (SNR) is then calculated as follows:

$$\text{SNR} = \frac{S}{\sqrt{p^2 + D^2 + R^2}}, \quad (4)$$

where S is the number of incident signal photoelectrons which in the cases analyzed will be the photons determined from synthetic spectral signal. The SNR is calculated for the peak intensity of the simulated spectra and also at ±0.5 Å from the peak intensity wavelength. It is required to have an idea about the signal strength at ±0.5 Å as it will be helpful to determine sufficient signal requirements near the wings of the spectral line for obtaining a better fit.

3.1 Slit Width Optimization

It was reported by Singh et al. (2019) that the slit width of VELC needs to be increased for achieving the desired scientific goals. For obtaining an optimized value of slit width, we used the synthetic spectra for analysis. The synthetic spectra were generated for a quiet-Sun condition, considering an average coronal temperature of $10^{6.25}$ K for the heights ranging from 1.1 to 1.5 $R_\odot$ in steps of 0.1 $R_\odot$. The emission measure and electron density for simulation using the coronal parameters (Baumbach, 1937; Allen, 1973) at these five heights are as follows:

TABLE 1 | Optimization of the slit width using the SNR calculations for slit widths of 20, 40, and 60 μm for log(T) = 6.25. The parameters peak and peak + scatter are in the unit of photoelectrons/pixel/second.

	Distance ($R_\odot$)	1.1	1.2	1.3	1.4	1.5
Slit width = 20 μm						
5,303 Å	Peak	659	182	80	41	25
	Peak + scatter	720	223	110	65	43
	SNR (peak)	21.39	8.56	4.34	2.39	1.512
	SNR (± 0.5 Å)	6.71	2.22	1.02	0.56	0.37
7,892 Å	Peak	53	17	9	5	3
	Peak + scatter	120	62	42	31	23
	SNR (peak)	3.15	1.08	0.58	0.33	0.19
	SNR (± 0.5 Å)	1.5	0.53	0.31	0.18	0.13
10,747 Å	Peak	14,349	5,439	2,820	1,619	1,041
	Peak + scatter	16,212	6,681	3,731	2,344	1,593
	SNR (peak)	113.02	64.06	41.63	27.82	19.64
	SNR (± 0.5 Å)	95.48	52.01	33.02	21.68	15.31
Slit width = 40 μm						
5,303 Å	Peak	1,287	355	155	80	48
	Peak + scatter	1,409	436	215	128	84
	SNR (peak)	31.79	13.76	7.35	4.23	2.71
	SNR (± 0.5 Å)	11.5	4.09	1.95	1.05	0.66
7,892 Å	Peak	104	34	17	9	6
	Peak + scatter	237	123	82	61	46
	SNR (peak)	5.69	2.09	1.08	0.58	0.39
	SNR (± 0.5 Å)	2.65	0.98	0.51	0.29	0.18
10,747 Å	Peak	28,018	10,620	5,506	3,161	2,033
	Peak + scatter	31,744	13,104	7,328	4,610	3,137
	SNR (peak)	162.34	95.41	64.55	45.02	32.97
	SNR (± 0.5 Å)	137.81	77.52	50.88	34.54	25.15
Slit width = 60 μm						
5,303 Å	Peak	1,861	513	224	115	69
	Peak + scatter	2,043	635	313	186	123
	SNR (peak)	39.04	17.45	9.62	5.64	3.67
	SNR (± 0.5 Å)	15.76	6.28	2.94	1.59	1.03
7,892 Å	Peak	152	50	24	14	9
	Peak + scatter	351	183	121	92	68
	SNR (peak)	7.78	2.99	1.51	0.89	0.58
	SNR (± 0.5 Å)	3.63	1.37	0.71	0.39	0.29
10,747 Å	Peak	40,476	15,342	7,954	4,567	2,937
	Peak + scatter	46,065	19,068	10,686	6,741	4,593
	SNR (peak)	196.93	117.28	80.66	57.37	42.81
	SNR (± 0.5 Å)	168.1	95.62	63.60	43.80	32.37

- log(EM) = [27, 26.3, 25.8, 25.36, and 25]
- log(n_e) = [8.2, 7.85, 7.6, 7.38, and 7.2].

The spectra were generated for the three channels at the five heights including the scattered intensity and noises. The SNR per pixel per second at the peak intensity and at ±0.5 Å from the peak intensity wavelength were calculated for different slit widths and are tabulated in **Table 1**.

It can be seen from **Table 1** that as the slit width is increased, there is an improvement in the SNR of all the channels. The increased SNR is also observed at the wings of the spectral line used for analysis. However, it should be noted that there has also been an increase in the number of photons incident on the detector. Increasing the number of incident photons also imposes the challenge of attaining sufficient SNR without saturating the detector. The CMOS sensors used for the visible spectral channels have a full well capacity of ~30,000 electrons in both high and low gain, whereas for INGAS (InGaS) used for the IR detector, it is ~30,300 electrons in the high-gain mode (Singh et al., 2019). The IR channel is also equipped with a spectropolarimeter mode which will operate in the high-gain mode with a fixed exposure time of 500 ms. When operated in this mode, it can be noted from **Table 1** that for a slit width of 60 μm, the incident photons count to ~23,033 electrons at 1.1 $R_\odot$, which is ~77% of the full well capacity. Thus, the slit width needs to be $\leq$ 60 μm. Therefore, we tested the SNR with a 50 μm slit width, keeping rest of the parameters the same as above. The results are shown in **Table 2**.

It can also be noticed from **Table 2** that

1) With a slit width of 50 μm, the IR spectropolarimeter mode could get an incident photon count of 19,540 at 1.1 $R_\odot$, having sufficient SNR at the same time.
2) The slit width of 50 μm leads to a photon count contributing to ~ 65% of the full well capacity for the IR channel at 1.1 $R_\odot$ in the spectropolarimeter mode. This is a sufficient margin to account for the flaring conditions or intensity enhancement in the coronal structures.
3) The SNR at the peak and wings decreases with height for all the channels. This implies that subsequent frames may be added *post facto* to enhance the SNR.
4) SNR for the Fe XI (7,892 Å) channel is lower than that for the other two channels for the selected simulation parameters.

3.2 Effect of Temperature on SNR

As the corona contains plasma of different temperatures, after optimizing the slit width to 50 μm, we analyzed the effect of different plasma temperatures on the performance of the spectral channels. The spectra are synthesized for the three channels at a height of 1.1 $R_\odot$, taking the electron density as $10^{8.2}$ cm^{-3} and EM = 10^{27} cm^{-5}. The temperature is varied from log(T) = 6.0 to log(T) = 6.5 in steps of 0.1. The scattered intensity and noise introduced by the instrument are also added accordingly. The result is tabulated in **Table 3**. It is noticed that the three channels show maximum SNR corresponding to different temperatures. This directly implies the importance of these lines for temperature diagnostics of the corona. It could be noted that the 7,892 Å channel shows good SNR for relatively cool plasma

TABLE 2 | SNR for the three spectral channels of VELC for the optimized slit width of 50 μm for log(T) = 6.25.

Slit width = 50 μm						
	Distance ($R_\odot$)	1.1	1.2	1.3	1.4	1.5
5,303 Å	Peak	1,582	437	190	98	59
	Peak + scatter	1,734	539	265	157	104
	SNR (peak)	35.71	15.76	8.55	4.98	3.23
	SNR (± 0.5 Å)	13.64	4.99	2.46	1.35	0.82
7,892 Å	Peak	128	42	20	12	7
	Peak + scatter	294	153	101	77	56
	SNR (peak)	6.77	2.55	1.26	0.77	0.45
	SNR (± 0.5 Å)	3.16	1.15	0.61	0.34	0.23
10,747 Å	Peak	34,423	13,047	6,765	3,884	2,498
	Peak + scatter	39,080	16,152	9,042	5,695	3,878
	SNR (peak)	180.95	107.19	73.23	51.66	38.24
	SNR (± 0.5 Å)	154.01	87.22	57.71	39.51	29.02

TABLE 3 | Effect of different plasma temperatures on the SNRs of the VELC spectral channels estimated at 1.1 $R_\odot$.

Slit width = 50 μm							
	log(T)	**6.0**	**6.1**	**6.2**	**6.3**	**6.4**	**6.5**
5,303 Å	Peak	11	249	1,237	1,391	390	68
	Peak + scatter	163	401	1,389	1,543	542	220
	SNR (peak)	0.55	9.92	30.75	33.04	14.04	3.21
	SNR (± 0.5 Å)	0.05	1.76	9.98	13.81	6.02	1.48
7,892 Å	Peak	1,025	1,043	342	36	2	1
	Peak + scatter	1,191	1,209	508	202	168	167
	SNR (peak)	28.95	29.24	14.31	2.21	0.13	0.06
	SNR (± 0.5 Å)	12.63	14.97	7.04	0.98	0.05	0.05
10,747 Å	Peak	3,183	23,479	42,559	19,635	2,495	214
	Peak + scatter	7,840	28,136	47,216	24,292	7,152	4,871
	SNR (peak)	45.23	147.76	202.14	134.21	38.21	4.81
	SNR (± 0.5 Å)	25.65	117.75	172.51	110.26	23.67	2.37

TABLE 4 | SNR for the VELC spectral channels for a slit width of 50 μm, taking the line formation peak temperature for each channel.

Slit width = 50 μm						
	Distance ($R_\odot$)	**1.1**	**1.2**	**1.3**	**1.4**	**1.5**
5,303 Å log(T) = 6.27	Peak	1,611	486	209	110	65
	Peak + scatter	1,763	570	284	169	110
	SNR (peak)	36.1	17.19	9.22	5.51	3.53
	SNR (± 0.5 Å)	13.64	4.99	2.46	1.35	0.82
7,892 Å log(T) = 6.1	Peak	1,043	334	161	88	56
	Peak + scatter	1,209	445	242	153	105
	SNR (peak)	29.24	14.07	8.15	4.94	3.31
	SNR (± 0.5 Å)	14.97	6.31	3.40	2.03	1.32
10,747 Å log(T) = 6.2	Peak	42,559	16,095	8,331	4,777	3,070
	Peak + scatter	47,216	19,200	10,608	6,588	4,450
	SNR (peak)	202.14	120.42	82.90	59.04	44.13
	SNR (± 0.5 Å)	172.51	98.70	65.88	45.52	33.66

compared to the other channels as the corresponding Fe XI ion formation temperature is comparatively lower than that of the other two ions in consideration. Looking at the values of SNRs for the three channels in **Table 3** also reveals that if the studies using these three lines are combined, it will be helpful in investigating plasma over a wide range of temperatures.

We then synthesized the lines at their respective peak formation temperatures and proceeded as described above. The temperatures chosen are close to the peak line formation temperature for these lines, which are $10^{6.27}$, $10^{6.1}$, and $10^{6.2}$ K for 5,303, 7,892, and 10,747 Å, respectively (Allen, 1973). We synthesized these three spectral lines at heights ranging from 1.1 to 1.5 $R_\odot$ with emission measure and electron density as mentioned in **Section 3.1** for a slit width of 50 μm and considering the scatter and noise addition as for the previous cases. **Figure 1** shows such synthetic spectra as are expected to be observed by VELC at 1.1 $R_\odot$. The spectra also include added scatter and noise values from the instrument at this height. The results of this analysis for the mentioned heights are summarized in **Table 4**, which reveals the peak SNR at the line peak and at the wings. On comparison with **Table 2**, it could be seen that the observed line intensity will have a sufficient SNR up to larger distances for line emission corresponding to their peak temperatures for all the spectral channels. For the cases of 5,303 and 7,892 Å, when the SNR becomes ≤ 5, it could be enhanced by pixel or frame binning as required.

These cases have been simulated taking the isothermal corona with electron density calculated using the Baumbach model. As this coronal density model is based on white-light eclipse observations that include contributions from different temperatures, we used a temperature distribution to calculate the signal variation with height for the three channels. We then compared the densities obtained from the Baumbach model with the values using the following relation:

$$n_e = n_0 e^{-\left(\frac{r-1.1}{H}\right)}, \tag{5}$$

where n_0 is the electron density estimated at 1.1 $R_\odot$ using the Baumbach model and H is the scale height which is dependent on the temperature. Using the two estimates of the densities, we performed a chi-square analysis to obtain the maximum match between the two models (**Figure 2A**). We found that for log(T) = 6.1, density estimates using the two methods match well. Taking this as the peak value of temperature and a width of 0.3, we generated 150 random numbers with a Gaussian distribution, as shown in **Figure 2B**, to perform Markov chain Monte Carlo

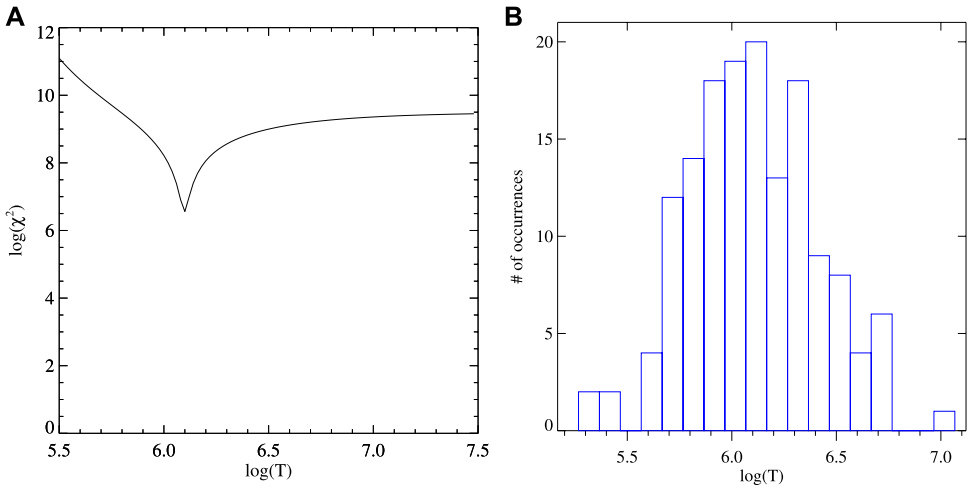

FIGURE 2 | (A) Chi-square minimization output as a function of temperature. **(B)** Temperature distribution with peak at log(T) = 6.1 used for MCMC simulation.

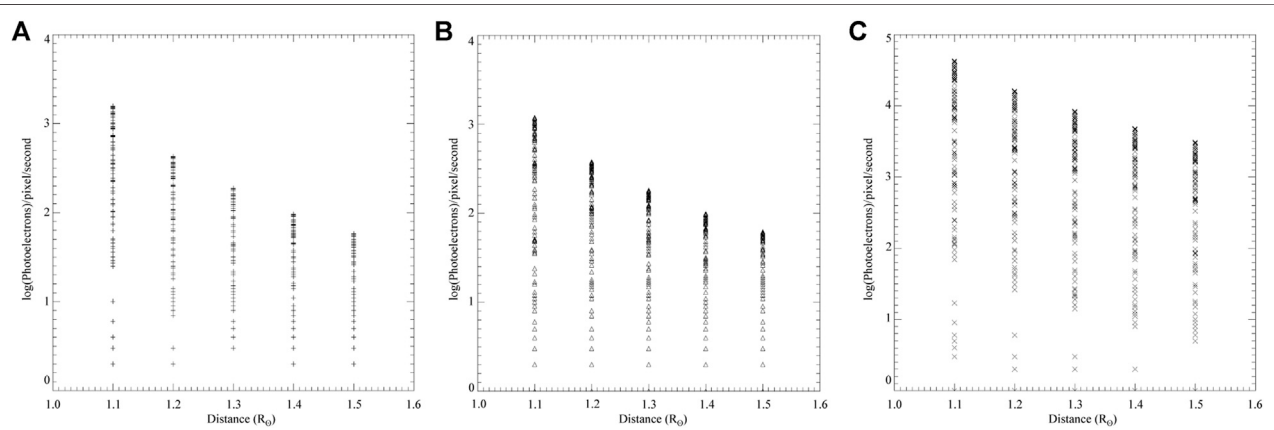

FIGURE 3 | Photoelectron variation using synthetic spectra for VELC at different heights for **(A)** 5,303 Å, **(B)** 7,892 Å, and **(C)** 10,747 Å for 50 μm slit width with temperature distribution. It should be noted that the counts for the IR channel are about an order of magnitude greater than those for the other two channels, as the IR sensor pixels are larger than the visible sensor pixels.

simulation (MCMC; Hastings, 1970), taking quiet-Sun densities and EM at the heights used previously with the 50 μm slit width.

We then estimated the photoelectrons generated in each pixel every second with temperature based on the distribution. The variation of the photoelectrons with height is shown in **Figure 3** for the three channels. It can be noted that there is a cluster of points near the top at each height for all channels. These values can be compared with the number of photoelectrons calculated at the line formation temperature for each channel, as specified in **Table 4**. Also, when the points in the clusters in **Figure 3** are compared with the counts tabulated in **Table 3**, we could infer that the spread near the peak counts in each channel is due to the contribution from the temperature close to the peak line formation temperatures for the respective lines. Thus, even though there is a range of counts available, from zero to thousands of photoelectrons each second, the maximum contribution will be observed due to the coronal structures contributing at and near the peak temperature for VELC channels.

3.3 Effect of CME on Spectra

We also analyzed the performance of the instrument for a case where CME is passing through spectrograph slits with a slit width of 50 μm. It should be noted that the ground-based coronagraph MLSO/KCor has an FOV similar to that of VELC. We used a CME case that was observed by KCor on 2016-01-01. A reference image for the locations of the slits in the VELC FOV in the spectral channels is shown in yellow, superimposed on the KCor image, as shown in **Figure 4A**. Due to the difference in the size of visible (2560 × 2160 pixels) and IR (640 × 512 pixels) channel detectors, the FOV covered is slightly different for the two. A circularly symmetric uniform coronal density based on the

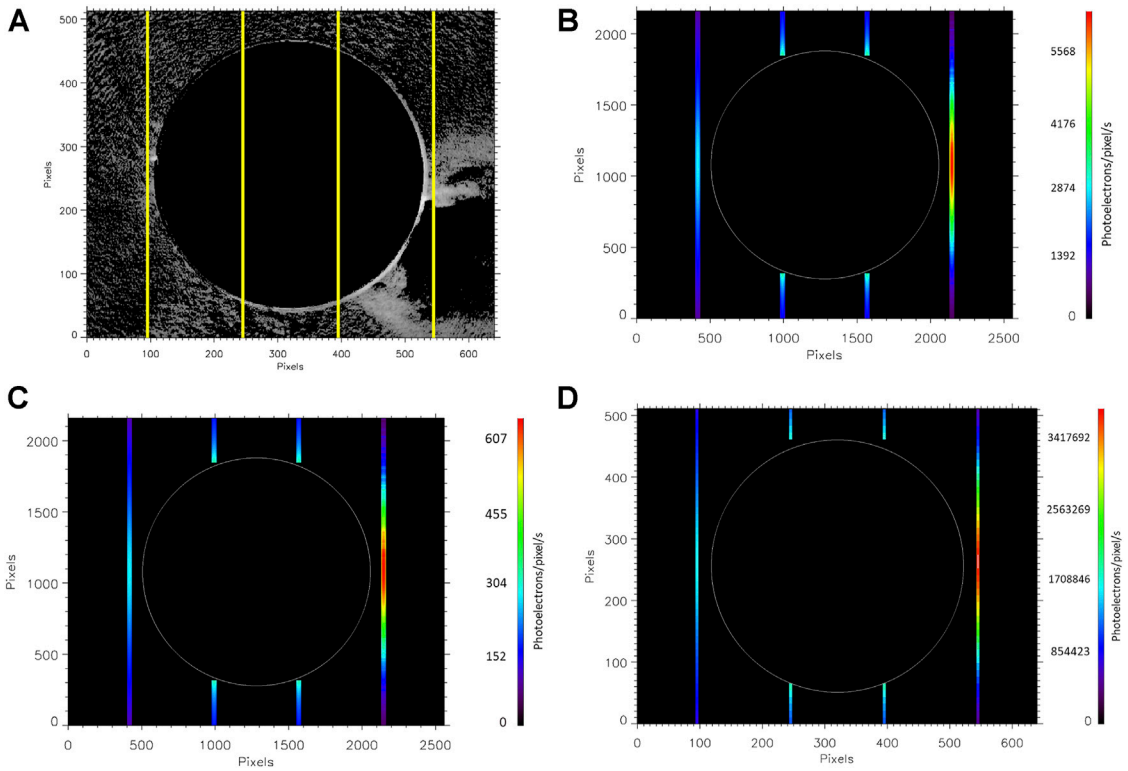

FIGURE 4 | (A) VELC slit locations overplotted in yellow on the KCor image of 2016-01-01 for the VELC FOV in the IR channel. **(B)**, **(C)**, and **(D)** Synthesized spectra for the four slits of VELC for 5,303, 7,892, and 10,747 Å, respectively. It could be noticed that in the region where CME is present, the intensity of the spectra is enhanced.

Baumbach model (Baumbach, 1937) was used for synthesizing the spectra. Since the white-light intensity is proportional to the electron density, we estimated the electron density by taking the ratio of the CME and non-CME images. The non-CME image used here was an average intensity image of the images prior to CME occurrence. The ratio provided an enhancement at the CME location with respect to the background corona. It was found that for this CME, the maximum enhancement attained was ~4 times above the background corona. This electron density was then used to synthesize the spectra at these locations with 1 s of exposure time. The emission measure value at 1.1 $R_\odot$ during the CME was taken as $10^{28.9}$ cm^{-5} due to CME which was varied up to 10^{25} cm^{-5} at the height of 1.5 $R_\odot$ with intermediate values interpolated using a third degree polynomial. It has been observed that the temperature of a CME can range from $10^{5.5}$ to $10^{6.5}$ K (Susino and Bemporad, 2016); hence, an average temperature of $10^{6.25}$ K was taken during the simulation of this case. The coronagraph slits are kept in the reference position with the center of the Sun lying midway between slits 2 and 3.

The synthetic spectra as will be observed by VELC corresponding to the 5,303, 7,892, and 10,747 Å channels are simulated and shown in **Figure 4**. Here, the center of slit 4 (from the left) is at a heliocentric distance of 1.11 $R_\odot$. In **Figures 4B–D**, the expected synthetic spectra for the CME seen in the reference image are shown, which will be observed by VELC at 5,303, 7,892, and 10,747 Å, respectively. It can be seen that at the location of the CME, there is an enhancement of peak intensity reflecting the increased electron density in the three channels of VELC. Comparing the peak electron counts in the presence of CME for the three channels with **Table 2**, it was found that there was an increment by ~4, ~5, and ~150 times for the 5,303, 7,892, and 10,747 Å channels, respectively. For the two visible channels, the electron count is sufficiently below the full well capacity of the detectors even after adding the scattered photons. However, for the IR channel, the counts are more than the full well detector capacity. This is due to the larger pixel size of the IR channel detector. This implies that even though exposure of more than 1 s could be set for the visible channels, it should be less than a second for the IR channel for CME observations to occur without saturating the detector. For this, when the CME is detected onboard using the onboard CME detection logic (Patel et al., 2018), the spectroscopic channel will be configured with a predetermined set of exposures. We plan to use the flag provided by the onboard CME detection algorithm for the continuum channel of VELC to change the IR observation to the low-gain mode with a reduced exposure time for CME observations.

3.4 SNR Requirements for Specific Cases

3.4.1 Magnetometry

One of the aims of VELC is the measurement of the coronal magnetic field using the IR channel of VELC. As the magnetic field in the active regions in the corona is of the order of a few tens

TABLE 5 | Variation of the Stokes-V signal, radially, in the VELC IR channel for a 50 μm slit width.

Distance ($R_\odot$)	**1.1**	**1.2**	**1.3**	**1.4**	**1.5**
V	35	13	7	4	3
I	26,164	9,894	5,121	2,937	1,887
% of polarization (V/I)	0.13194976	0.13195072	0.13195114	0.13195138	0.13195152

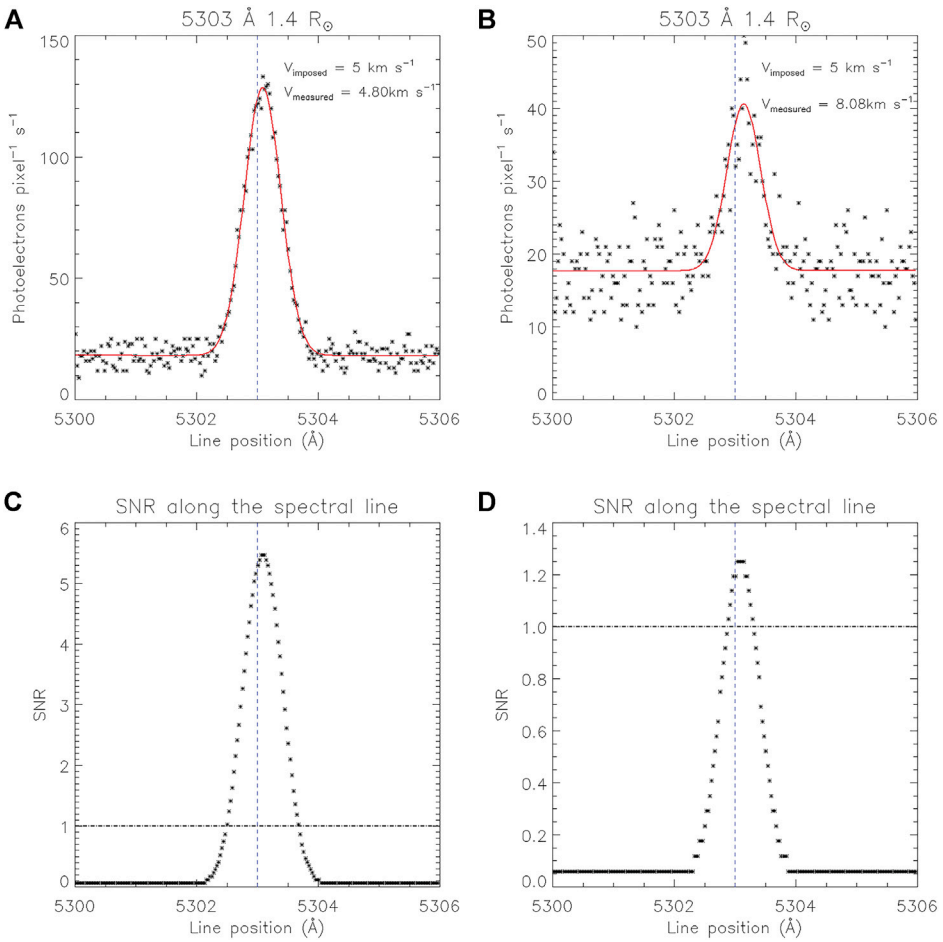

FIGURE 5 | Synthetic green line with noise and Doppler shift added **(A)** at 1.4 $R_\odot$ and **(B)** at 20% intensity of **(A)**. The vertical dashed line shows the rest wavelength. **(C)** and **(D)** show SNR variation within the spectral line, respectively, for **(A)** and **(B)** where the horizontal dotted-dashed line marks the SNR = 1.

of Gauss (Lin et al., 2000), we synthesized the weakest Stokes profile, V, for the intensity for the IR channel, keeping the EM and density the same as in the previous cases for a slit width of 50 μm and a temperature of $10^{6.2}$ K. The radial variation of the V signal for a magnetic field strength of 10 G is presented in **Table 5**. It could be noted that the V/I percentage of polarization for the instrument accounts to ~0.13%. Taking into account the Poisson noise at 1.1 $R_\odot$, the SNR will be ≈ 6. To perform the magnetic field measurement, the SNR for Stokes-V should be in the order of ~1,000. Acquiring this SNR requires integration times above one hour. Images with nominal exposure times will be recorded to avoid detector saturation and summed on the ground to produce sufficient SNR to provide critical measurements of the magnetic field in coronal active regions.

3.5 Doppler Maps

VELC will be used to produce Doppler maps to study the line-of-sight plasma motions in the solar corona. This will also be helpful in studying the turbulence generated in the corona. We used the synthetic spectra at a height of 1.4 $R_\odot$, where the SNR for 5,303 Å is ≈ 5 for the quiet-Sun case, as mentioned in **Table 4**. We then imposed a Doppler velocity of 5 km s^{-1}, resulting in a shift of ≈ 88 mÅ for the line peak from the rest wavelength position. We added the noise introduced in **Section 3** randomly along the

spectral line to mimic the near-realistic observation. The final spectra were then fitted with a Gaussian profile, and the Doppler velocity was then measured. **Figures 5A,B** show the synthetic spectra at 1.4 $R_\odot$ and with 20% counts of the prior. The vertical dashed line is the position of the rest wavelength for the spectra. The SNR variation within the line is shown in **Figures 5C,D**. It could be seen that when the SNR at the peak of the spectra is ≈ 5, a reliable Doppler speed is measured in the synthetic data that is close to the imposed one. On the other hand, when the SNR at the line peak is close to 1, a significant deviation could be seen in the measured Doppler speed (**Figure 5B**). We found that an SNR of at least 5 is good enough to measure a Doppler speed as low as 5 km s^{-1} using the green channel of VELC when all the noise sources are included in the line profile.

4 SUMMARY AND DISCUSSIONS

VELC onboard Aditya-L1 will provide a unique opportunity to simultaneously image and perform spectroscopic observations of the inner solar corona in three visible and one IR passband. It will be used for spectroscopic diagnostics of the corona up to 1.5 $R_\odot$ using three emission lines, 5,303, 7,892, and 10,747 Å. It is necessary to simulate the performance of the instrument that will be useful for designing the observation plan after the launch. In this work, we used synthetic spectral data to characterize the spectral channels of VELC for different solar conditions. We synthesized the spectra for the three channels using the CHIANTI atomic database, taking into account the instrument characteristics. We also added the contribution of the instrument, including the scattered intensity and detector noise, to the synthesized spectra. The scattered intensity available for the continuum channel of the instrument was scaled for the spectral channel parameters. The final spectra were then analyzed using the signal-to-noise ratio calculated at the line center wavelength and at ±0.5 Å from the line center.

We simulated the synthetic spectra taking the isothermal condition with average coronal temperature as $10^{6.25}$ K for the three channels and estimated the SNR for the emission lines at coronal heights from 1.1 to 1.5 $R_\odot$. For the simulation, the slit width was varied as 20, 40, and 60 μm. We found that on increasing the slit width, the SNR at the peak intensity and at the wings increased for all the three channels. It was identified that for the slit width of 60 μm, the detector for IR channels fills up to 77% of its capacity with 500 ms exposure in the high-gain mode to be used for the spectropolarimetery mode. In order to keep a modest margin for this particular mode, the analysis was done taking the slit width as 50 μm. It was found that a slit width of 50 μm leads to 65% filling of the IR detector in the spectropolarimeter mode, providing a sufficient SNR at the same time. Thus, based on the requirement for this particular mode, we believe that a slit width of 50 μm for the VELC spectral channels will be sufficient to study different regions of the solar atmosphere.

It can be seen from **Table 2** that the SNR for 7,892 Å is relatively poor compared to the other two. This is because different lines have different formation temperatures. Therefore, we also studied the effect of different coronal plasma temperatures on the performance of the VELC spectral channels for the optimized slit width. We synthesized the spectra for the three channels at 1.1 $R_\odot$, varying the temperature from log(T) = 6.0 to log(T) = 6.5 in steps of 0.1. We found that the SNR at the line peak varies with the change in temperature such that the maximum SNR observed for 5,303, 7,892, and 10,747 Å was at log(T) of 6.3, 6.1, and 6.2, respectively. These temperatures are close to their line formation temperatures. We could observe a similar increase in the SNR for the wings of the synthesized spectral lines. We analyzed the instrument's performance with a slit width of 50 μm to synthesize the spectra with their line formation temperatures. The SNR was then estimated at the line peak and the wings for coronal heights from 1.1 to 1.5 $R_\odot$. From the results of this analysis presented in **Table 4**, it could be observed that there is a sufficient SNR in all the channels for the line peak and the wings, which decreases at larger heights. The IR channel has a very good SNR even at larger heights due to its bigger pixel size compared to the other two.

As these analyses were based on isothermal coronal conditions, we also used an MCMC simulation taking a Gaussian distribution of temperature peaking at $10^{6.1}$ K having a width of $10^{0.3}$ K to estimate the expected signal at different heights in the VELC FOV. We found that there is a spread in the estimated counts based on the temperature distribution, with a cluster obtained corresponding to the temperatures close to the line formation temperature for individual channels (**Figure 3**). Overall analysis shows that for the optimized slit width of 50 μm and considering the peak line formation temperatures of each line, a reliable signal could be obtained for all the channels which could be used for analysis. For the larger heights, when the SNR becomes ≤ 5, pixel binning could be considered to enhance the signal with respect to the background. There is also an option to increase the exposure time without saturating the detector, which could also boost the signal. For the study of very fast transients requiring short exposure times, the observations could be taken at a high cadence. Such short exposure frames could be further binned to increase the SNR.

We also performed a study of a CME case approximating the enhanced electron density due to a CME of 2016-01-01 from KCor images, which has a similar FOV as VELC. We found that the visible spectral channels of VELC could be operated for CME observations with an exposure time more than 1 s, whereas the IR channel will be operated in the low-gain mode following the trigger provided by the onboard CME detection algorithm with a reduced exposure time. More CME cases could be analyzed in the future with different enhancements that could help in planning for spectral diagnostics of CMEs using VELC. We also considered two specific scientific cases, magnetometry and Doppler mapping, with regards to the SNR requirement from a VELC point of view. For the measurement of the magnetic field using the IR channel, we calculated the Stokes-V intensity, thereby estimating the minimum integration time required. For the Doppler mapping, we used the green line at a height of 1.4 $R_\odot$, where SNR ≈ 5. We also considered a case where the intensity of the line is 20% of the case mentioned above. For the two

cases, we added the noise and a Doppler speed, which were measured later by fitting a Gaussian profile. We found that a minimum SNR of 5 will be required for Doppler mapping using VELC.

It should be noted that increasing the slit width results in the broadening of the spectral lines and hence a reduction in the spectral resolution. Singh et al. (2019) studied the effect of increasing the slit width for the three spectral channels of VELC. Their analysis also indicates that the slit width should be increased to enhance the SNR at the same time, optimizing the spectral resolution to meet the scientific requirements. These estimates will be helpful in identifying the expected observed spectra including the instrument contribution, which could be deconvolved during the processing to get the true line profile. The effect of spacecraft drift and jitter as studied by Ranganathan and Sankarasubramanian (2019) has not been considered for the studies presented here but will be included in our future work. Such complete spectral information will be helpful for the data pipeline development and extracting the signal from the background.

In this work, we have presented a few of the solar conditions. A similar study could be extended to other solar features such as loops, plumes, and coronal holes which result in different ambient coronal conditions. Such extensive studies covering different cases could help in preparing the optimized plan for maximizing the science output from the instrument. It should be noted that this study could also be extended to future missions, which include spectrographs for preparing the target science cases that could be addressed with the instrument capabilities.

DATA AVAILABILITY STATEMENT

The raw data supporting the conclusions of this article will be made available by the authors, without undue reservation.

AUTHOR CONTRIBUTIONS

AM, MV, and AS generated the synthetic spectra for different solar conditions using the CHIANTI database, taking the instrument parameters. RP and MV converted the synthesized spectra to the instrument's synthetic observations. RP carried out the estimations and prepared the manuscript. KS and DB planned the analysis from the observational point of view. VP provided the essential inputs to analyze the results. All authors took part in the discussion.

ACKNOWLEDGMENTS

We would like to acknowledge IIA, ISRO, and ARIES for providing the necessary facilities and computation requirements. We thank the VELC instrument team for providing the instrument parameters when required. We also thank the CHIANTI team for making the database available. RP and AS would like to thank Samrat Sen for discussions regarding the analysis. RP, AM, and MV were supported by DST. CHIANTI is a collaborative project involving the University of Cambridge (United Kingdom), the NASA Goddard Space Flight Center (United States), the George Mason University (GMU, United States), and the University of Michigan (United States).

REFERENCES

Allen, C. W. (1973). *Astrophysical Quantities*.

Banerjee, D., Patel, R., and Pant, V. (2017). The Inner Coronagraph on Board Aditya-L1 and Automatic Detection of Cmes. *Proc. IAU.* 13, 340–343. doi:10.1017/S1743921317008584

Baumbach, S. (1937). Strahlung, ergiebigkeit und elektronendichte der sonnenkorona. *Astr. Nachr.* 263, 121–134. doi:10.1002/asna.19372630602

Boe, B., Habbal, S., Druckmüller, M., Landi, E., Kourkchi, E., Ding, A., et al. (2018). The First Empirical Determination of the Fe10+ and Fe13+ Freeze-In Distances in the Solar Corona. *Astrophys. J.* 859, 155. doi:10.3847/1538-4357/aabfb7

Culhane, J. L., Harra, L. K., James, A. M., Al-Janabi, K., Bradley, L. J., Chaudry, R. A., et al. (2007). The EUV Imaging Spectrometer for Hinode. *Sol. Phys.* 243, 19–61. doi:10.1007/s01007-007-0293-1

De Pontieu, B., Title, A. M., Lemen, J. R., Kushner, G. D., Akin, D. J., Allard, B., et al. (2014). The Interface Region Imaging Spectrograph (IRIS). *Solar Phys.* 289, 2733–2779. doi:10.1007/s11207-014-0485-y

Del Zanna, G., Dere, K. P., Young, P. R., Landi, E., and Mason, H. E. (2015). CHIANTI - an Atomic Database for Emission Lines. Version 8. *Astron. Astrophys.* 582, A56. doi:10.1051/0004-6361/201526827

Dere, K. P., Landi, E., Mason, H. E., Monsignori Fossi, B. C., and Young, P. R. (1997). CHIANTI - an Atomic Database for Emission Lines. *Astron. Astrophys. Suppl. Ser.* 125, 149–173. doi:10.1051/aas:1997368

Fan, S., He, J., Yan, L., Tomczyk, S., Tian, H., Song, H., et al. (2018). Turbulence and Heating in the Flank and Wake Regions of a Coronal Mass Ejection. *Sol. Phys.* 293, 6. doi:10.1007/s11207-017-1221-1

Habbal, S. R., Druckmüller, M., Morgan, H., Daw, A., Johnson, J., Ding, A., et al. (2010). Mapping the Distribution of Electron Temperature and Fe Charge States in the Corona with Total Solar Eclipse Observations. *Astrophys. J.* 708, 1650–1662. doi:10.1088/0004-637X/708/2/1650

Habbal, S. R., Druckmüller, M., Morgan, H., Ding, A., Johnson, J., Druckmüllerová, H., et al. (2011). Thermodynamics of the Solar Corona and Evolution of the Solar Magnetic Field as Inferred from the Total Solar Eclipse Observations of 2010 July 11. *Astrophys. J.* 734, 120. doi:10.1088/0004-637X/734/2/120

Habbal, S. R., Morgan, H., and Druckmüller, M. (2014). EXPLORING THE PROMINENCE-CORONA CONNECTION AND ITS EXPANSION INTO THE OUTER CORONA USING TOTAL SOLAR ECLIPSE OBSERVATIONS. *Astrophys. J.* 793, 119. doi:10.1088/0004-637x/793/2/119

Habbal, S. R., Morgan, H., Johnson, J., Arndt, M. B., Daw, A., Jaeggli, S., et al. (2007). Localized Enhancements of Fe+10Density in the Corona as Observed in Fexi789.2 Nm during the 2006 March 29 Total Solar Eclipse. *Astrophys. J.* 663, 598–609. doi:10.1086/518403

Hastings, W. K. (1970). Monte Carlo Sampling Methods Using Markov Chains and Their Applications. *Biometrika.* 57, 97–109. doi:10.1093/biomet/57.1.97

Kumar, N. R., Prasad, B. R., Singh, J., and Venkata, S. (2018). Optical Design of Visible Emission Line Coronagraph on Indian Space Solar mission Aditya-L1. *Exp. Astron.* 45, 219–229. doi:10.1007/s10686-017-9569-7

Lin, H., Penn, M. J., and Tomczyk, S. (2000). A New Precise Measurement of the Coronal Magnetic Field Strength. *Astrophys. J. Lett.* 541, L83–L86. doi:10.1086/312900

McIntosh, S. W., and De Pontieu, B. (2012). Estimating the "Dark" Energy Content of the Solar Corona. *Astrophys. J.* 761, 138. doi:10.1088/0004-637X/761/2/138

Morgan, H., and Habbal, S. R. (2007). The Long-Term Stability of the Visible F corona at Heights of 3-6R\odot. *Astronomy & Astrophysics.* 471, L47–L50. doi:10.1051/0004-6361:20078071

Morton, R. J., Tomczyk, S., and Pinto, R. F. (2016). A GLOBAL VIEW OF VELOCITY FLUCTUATIONS IN THE CORONA BELOW 1.3R⊙WITH CoMP. *Astrophys. J.* 828, 89. doi:10.3847/0004-637X/828/2/89

Morton, R. J., Tomczyk, S., and Pinto, R. (2015). Investigating Alfvénic Wave Propagation in Coronal Open-Field Regions. *Nat. Commun.* 6, 7813. doi:10.1038/ncomms8813

Morton, R. J., Weberg, M. J., and McLaughlin, J. A. (2019). A Basal Contribution from P-Modes to the Alfvénic Wave Flux in the Sun's corona. *Nat. Astron.* 3, 223–229. doi:10.1038/s41550-018-0668-9

Pant, V., Magyar, N., Van Doorsselaere, T., and Morton, R. J. (2019). Investigating "Dark" Energy in the Solar Corona Using Forward Modeling of MHD Waves. *Astrophys. J.* 881, 95. doi:10.3847/1538-4357/ab2da3

Pasachoff, J. M., Babcock, B. A., Russell, K. D., and Seaton, D. B. (2002). Short-Period Waves that Heat the Corona Detected at the 1999 Eclipse. *Solar Phys.* 207, 241–257. doi:10.1023/A:1016297800478

Patel, R., Amareswari, K., Pant, V., Banerjee, D., Sankarasubramanian, K., and Kumar, A. (2018). Onboard Automated Cme Detection Algorithm for the Visible Emission Line Coronagraph on Aditya-L1. *Sol. Phys.* 293, 103. doi:10.1007/s11207-018-1323-4

Prasad, S. K., Singh, J., and Ichimoto, K. (2013). Thermal Structure of Coronal Loops as Seen with Norikura Coronagraph. *Astrophys. J.* 765, L46. doi:10.1088/2041-8205/765/2/L46

Raghavendra Prasad, B., Banerjee, D., Singh, J., Nagabhushana, S., Kumar, A., Kamath, P. U., et al. (2017). Visible Emission Line Coronagraph on Aditya-L1. *Curr. Sci.* 113, 613–615. doi:10.18520/cs/v113/i04/613-615

Ranganathan, M., and Sankarasubramanian, K. (2019). Polarimeter for Coronal Magnetic Field Measurement: Design and Evaluation of Polarization Cross Talk. *J. Astronomical Telescopes, Instr. Syst.* 5, 044003. doi:10.1117/1.jatis.5.4.044003

Sakurai, T., Ichimoto, K., Raju, K. P., and Singh, J. (2002). Spectroscopic Observation of Coronal Waves. *Solar Phys.* 209, 265–286. doi:10.1023/A:1021297313448

Samanta, T., Singh, J., Sindhuja, G., and Banerjee, D. (2016). Detection of High-Frequency Oscillations and Damping from Multi-Slit Spectroscopic Observations of the Corona. *Sol. Phys.* 291, 155–174. doi:10.1007/s11207-015-0821-x

Seetha, S., and Megala, S. (2017). Aditya-L1 mission. *Curr. Sci.* 113, 610–612. doi:10.18520/cs/v113/i04/610-612

Singh, J., Bayanna, R., and Sankarasubramanian, K. (2013). Visible Emission Line Space Solar Coronagraph: Science and Optical Design. *J. Opt.* 42, 96–100. doi:10.1007/s12596-012-0115-8

Singh, J., Cowsik, R., Raveendran, A. V., Bagare, S. P., Saxena, A. K., Sundararaman, K., et al. (1997). Detection of Short-Period Coronal Oscillations during the Total Solar Eclipse of 24 October, 1995. *Solar Phys.* 170, 235–252. doi:10.1023/A:1004943924584

Singh, J., Hasan, S. S., Gupta, G. R., Nagaraju, K., and Banerjee, D. (2011). Spectroscopic Observation of Oscillations in the Corona during the Total Solar Eclipse of 22 July 2009. *Sol. Phys.* 270, 213–233. doi:10.1007/s11207-011-9732-7

Singh, J., Ichimoto, K., Sakurai, T., and Muneer, S. (2003). Spectroscopic Studies of the Solar corona. IV. Physical Properties of Coronal Structure. *Astrophys. J.* 585, 516–523. doi:10.1086/346000

Singh, J., Raghavendra Prasad, B., Suresh Venkata, S., and Amit Kumar, A. (2019). Exploring the Outer Emission corona Spectroscopically by Using Visible Emission Line Coronagraph (VELC) on Board ADITYA-L1 mission. *Adv. Space Res.* 64, 1455–1464. doi:10.1016/j.asr.2019.07.007

Singh, J., Sakurai, T., and Ichimoto, K. (2006a). Do the Line Widths of Coronal Emission Lines Increase with Height above the Limb? *Astrophys. J.* 639, 475–483. doi:10.1086/499200

Singh, J., Sakurai, T., Ichimoto, K., Muneer, S., and Raveendran, A. V. (2006b). Spectroscopic Studies of Solar Corona VIII. Temperature and Non-Thermal Variations in Steady Coronal Structures. *Sol. Phys.* 236, 245–262. doi:10.1007/s11207-006-0104-7

Singh, J., Sakurai, T., Ichimoto, K., and Watanabe, T. (2004). Complex Variations in the Line-Intensity Ratio of Coronal Emission Lines with Height above the Limb. *Astrophys. J.* 617, L81–L84. doi:10.1086/427078

SPICE Consortium, Anderson, M., Appourchaux, T., Auchère, F., Aznar Cuadrado, R., Barbay, J., et al. (2020). The Solar Orbiter Spice Instrument - an Extreme Uv Imaging Spectrometer. *A&A*. 642, A14. doi:10.1051/0004-6361/201935574

Stix, M. (2002). *The Sun*. Berlin, Heidelberg: Springer. doi:10.1007/978-3-642-56042-2

Susino, R., and Bemporad, A. (2016). DETERMINATION OF CORONAL MASS EJECTION PHYSICAL PARAMETERS FROM A COMBINATION OF POLARIZED VISIBLE LIGHT AND UV LyαOBSERVATIONS. *Astrophys. J.* 830, 58. doi:10.3847/0004-637X/830/2/58

Tiwari, A. K., Morton, R. J., Régnier, S., and McLaughlin, J. A. (2019). Damping of Propagating Kink Waves in the Solar Corona. *Astrophys. J.* 876, 106. doi:10.3847/1538-4357/ab164b

Tomczyk, S., Card, G. L., Darnell, T., Elmore, D. F., Lull, R., Nelson, P. G., et al. (2008). An Instrument to Measure Coronal Emission Line Polarization. *Sol. Phys.* 247, 411–428. doi:10.1007/s11207-007-9103-6

Tomczyk, S., McIntosh, S. W., Keil, S. L., Judge, P. G., Schad, T., Seeley, D. H., et al. (2007). Alfven Waves in the Solar Corona. *Science*. 317, 1192–1196. doi:10.1126/science.1143304

van de Hulst, H. C. (1950). The Electron Density of the Solar corona. *Bull. Astronomical Institutes Neth.* 11, 135

Venkata, S. N., Prasad, B. R., Nalla, R. K., and Singh, J. (2017). Scatter Studies for Visible Emission Line Coronagraph on Board ADITYA-L1 mission. *J. Astronomical Telescopes, Instr. Syst.* 3, 014002. doi:10.1117/1.jatis.3.1.014002

Yang, Z., Bethge, C., Tian, H., Tomczyk, S., Morton, R., Del Zanna, G., et al. (2020). Global Maps of the Magnetic Field in the Solar corona. *Science*. 369, 694–697. doi:10.1126/science.abb4462

Conflict of Interest: The authors declare that the research was conducted in the absence of any commercial or financial relationships that could be construed as a potential conflict of interest.